AIAA JOURNAL
Vol. 56, No. 12, December 2018

High-Order Variational Multiscale Model in Finite Elements Applied to the LEISA-2 Configuration

Pierre Yser*
Dassault Aviation, 92214 Saint-Cloud, France
and
Christophe Bailly†
University of Lyon, École Centrale de Lyon, 69134 Écully, France

DOI: 10.2514/1.J057090

A variational multiscale sugbrid model including an explicit filtering is studied in the framework of an equal-order finite element formulation for solving compressible Navier–Stokes equations in entropy variables. The filtering is here achieved by considering embedded piecewise polynomials, whose implementation is made easier with the use of isoparametric and symmetric elements. A hybrid formulation combining a detached-eddy simulation near the walls is also proposed to be able to tackle realistic industrial configurations. The numerical developments are assessed with the Taylor–Green vortex, by comparison with a reference result provided by direct numerical simulation. Finally, new findings are reported with the direct noise computation of the LEISA-2 configuration, a three-element high-lift airfoil as part of the benchmark for airframe noise computation.

Nomenclature

$\underline{\underline{\boldsymbol{A}}}_i$	=	Jacobian matrix of Euler flux
$\underline{\underline{\boldsymbol{A}}}_0$	=	change of variables matrix
$\underline{\underline{\boldsymbol{K}}}_{ij}$	=	diffusive matrix
k	=	wave number, m^{-1}
n_n	=	number of nodes (mesh)
O_i	=	interpolation functions of ith spatial order
p	=	pressure, Pa
T	=	temperature, K
$\underline{\underline{\mathbb{T}}}$	=	subgrid-scale tensor
$\boldsymbol{U}$	=	conservative variables
$\boldsymbol{u}$	=	(u, v, w), velocity vector and its components, m/s
$\boldsymbol{V}$	=	entropy variables
$\boldsymbol{x}$	=	spatial coordinates, m
Δ	=	mean local length scale (element, filter), m
ν	=	kinematic viscosity, m^2/s
ρ	=	mass density, kg/m^3
Ω	=	volume of the computational domain, m^3

Superscripts

$\boldsymbol{u}^R$	=	resolved velocity field (LES), the velocity being $\boldsymbol{u}^R + \boldsymbol{u}'$
$\boldsymbol{u}'$	=	unresolved field
$\mathring{\boldsymbol{u}}$	=	low-wavenumber filtered field (VMS), the resolved field being $\mathring{\boldsymbol{u}} + \boldsymbol{u}''$
$\overline{\boldsymbol{u}^R}$	=	mean resolved field, the resolved field being $\overline{\boldsymbol{u}^R} + \boldsymbol{u}^*$
$\boldsymbol{u}^*$	=	resolved fluctuating field
$\boldsymbol{u}''$	=	high-wave-number filtered field (variational multiscale)

I. Introduction

LARGE-EDDY simulation (LES) is currently an effective approach to investigate realistic aeronautical problems such as the flight envelope limits of an aircraft, frequently characterized by large regions of separated flows, and the prediction of aerodynamic noise. The equations to be solved are obtained by applying a spectral low-pass filter in the space domain to the compressible Navier–Stokes equation. The smallest turbulent scales are filtered out, and the effects of these subgrid scales are usually modeled by a turbulent viscosity. A high additional numerical cost has to be paid, however, for the simulation of wall-bounded turbulent flows. Detached-eddy simulation (DES) provides an attractive alternative technique in this context. The unsteady Reynolds-averaged Navier–Stokes (RANS) equations are solved near the wall based on a statistical turbulence model, whereas a formal large-eddy simulation is performed elsewhere. Various clever models have been proposed in the literature [1]. The most classical formulation is based on the Spalart–Allmaras statistical model [2] combined with a Smagorinsky model for the large-eddy simulation, and it is known [3,4] as the delayed detached-eddy simulation model (DDES).

In parallel with these developments, much progress has been made in LES modeling, in particular by implementing a more explicit separation of spatial scales. The focus here is on variational multiscale methods introduced by Hughes et al. [5–7] in the framework of unstructured meshes and in continuity with the recent work by Sagaut and Levasseur [8] and Levasseur et al. [9]. Using the entropy variables, the symmetrized compressible Navier–Stokes equations are solved by a semidiscrete Galerkin/least-squares formulation associated with an implicit time-integration. The small scales are then identified through a variational projection, and the best results have been obtained by using a hyperviscosity subgrid-scale model [9]. A square matrix of size the number of nodes must, however, be inverted to compute the filtered field. A mass lumping technique has been introduced by these authors to reduce the numerical cost. The properties of the filter are unfortunately deteriorated by this approximation, in particular when the filter order is increased.

The aim of the present study is to investigate a variational multiscale (VMS) method for large-eddy simulation including an explicit filtering for the two-band decomposition, but the view taken to calculate the filtered field differs from the previous contributions. The filtering procedure is here based on embedded polynomial interpolation functions, can be applied to a mere linear element, and can also be naturally extended to high-order elements. Moreover, a hybrid formulation is proposed combining the new explicit filtering and the VMS model on the one hand, and a DDES formulation near the walls on the other hand, to tackle realistic industrial applications, as illustrated with the noise of a high-lift aerofoil in this study. There is a strong motivation for improving the accuracy of the flow description in this region [10], in particular for aeroacoustic

Received 6 January 2018; revision received 14 June 2018; accepted for publication 21 July 2018; published online 22 October 2018.

*Research and Development Engineer, Aerodynamics Department; pierre.yser@dassault-aviation.com.

†Professor, Laboratoire de Mécanique des Fluides de d'Acoustique, UMR CNRS 5509; christophe.bailly@ec-lyon.fr. Senior Member AIAA.

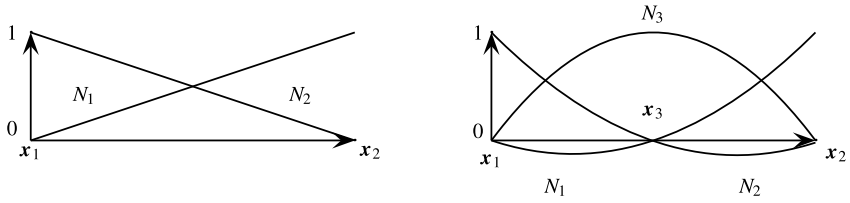

Fig. 1 Interpolation functions O_1 on the left and O_2 on the right.

applications when wall pressure fluctuations are used as input in an integral equation.

The paper is organized as follows. The Galerkin least-squares finite element method and the VMS model are first described in Sec. II for the entropy variables. In addition, the new procedure to calculate the filtered fields and the hybrid formulation are presented. The Taylor–Green vortices have been retained to assess the new VMS model, and LES numerical results are reported in Sec. III. Finally, the noise of a three-element high-lift airfoil introduced in the framework of the benchmark for airframe noise computation [11] is considered. This LEISA-2 problem allows to illustrate the benefits of the new developments for a realistic simulation in aeronautics but also to report new findings.

II. Numerical Method

A. Governing Equations in Terms of Entropy Variables

The flow is assumed to be compressible, and air is considered as a perfect gas in local thermodynamic equilibrium. The fluid is Newtonian, the bulk viscosity is neglected, and the thermal flux is provided by Fourier's law. The Navier–Stokes equation reformulated in a matrix form reads

$$\boldsymbol{U}_{,t} + \underline{\underline{\boldsymbol{A}}}_i \boldsymbol{U}_{,i} = \left(\underline{\underline{\boldsymbol{K}}}_{ij} \boldsymbol{U}_{,j}\right)_{,i} \tag{1}$$

where $\boldsymbol{U} = (\rho, \rho\boldsymbol{u}, \rho e_t)$ represents the conservative variables (ρ is the density, $\boldsymbol{u}$ is the velocity vector, and e_t is the total energy); $\underline{\underline{\boldsymbol{A}}}_i$ is the Jacobian matrix of Eulerian flux in the ith direction; and $\underline{\underline{\boldsymbol{K}}}_{ij}$ is the diffusive matrix. The index preceded by a comma denotes a partial derivative. The conservative formulation (1) is not well suited for numerical simulations in finite elements. An entropy formulation of the compressible Navier–Stokes equation is preferred [12,13], leading to a problem recast into a matrix form involving only symmetrical and positive definite matrices. By considering the generalized entropy function defined by $\mathcal{H}(\boldsymbol{U}) = -\rho s$, where s is the entropy, and the change of variables $\boldsymbol{V} = (\partial\mathcal{H}/\partial\boldsymbol{U})$, the Navier–Stokes equation (1) can be reformulated as [9]

$$\widetilde{\underline{\underline{\boldsymbol{A}}}}_0 \boldsymbol{V}_{,t} + \widetilde{\underline{\underline{\boldsymbol{A}}}}_i \boldsymbol{V}_{,i} = \left(\widetilde{\underline{\underline{\boldsymbol{K}}}}_{ij} \boldsymbol{V}_{,j}\right)_{,i} \tag{2}$$

The Jacobian matrix $\widetilde{\underline{\underline{\boldsymbol{A}}}}_0 = \boldsymbol{U}_{,\boldsymbol{V}}$ is associated with the change of variables; the flux vectors are given by $\widetilde{\underline{\underline{\boldsymbol{A}}}}_i = \underline{\underline{\boldsymbol{A}}}_i \widetilde{\underline{\underline{\boldsymbol{A}}}}_0$ and $\widetilde{\underline{\underline{\boldsymbol{K}}}}_{ij} = \underline{\underline{\boldsymbol{K}}}_{ij} \widetilde{\underline{\underline{\boldsymbol{A}}}}_0$; and the unknown vector is $\boldsymbol{V} = (1/T)(h - Ts - \|\boldsymbol{u}\|^2/2, \boldsymbol{u}, -1)$, where h is the enthalpy, and T is the temperature. The cumbersome expression of all theses matrices is not repeated here [9,12].

B. Finite Element Algorithm

Equation (2) is solved with a finite element method [14] implemented in the in-house solver AETHER developed by Dassault Aviation. A description of the flow solver can be found in Chalot and Perrier [15]. In what follows, only the main steps of the numerical algorithm are introduced. The variational formulation is obtained by multiplying Eq. (2) with weighting functions $\boldsymbol{W}$ chosen in the same functional space as the unknown vector $\boldsymbol{V}$, that is

$$\int_\Omega \boldsymbol{W} \cdot \left[\widetilde{\underline{\underline{\boldsymbol{A}}}}_0 \boldsymbol{V}_{,t} + \widetilde{\underline{\underline{\boldsymbol{A}}}}_i \boldsymbol{V}_{,i} - \left(\widetilde{\underline{\underline{\boldsymbol{K}}}}_{ij} \boldsymbol{V}_{,j}\right)_{,i}\right] \mathrm{d}\Omega = 0 \tag{3}$$

where $\widetilde{\underline{\underline{\boldsymbol{A}}}}_0 \boldsymbol{V}_{,t} + \widetilde{\underline{\underline{\boldsymbol{A}}}}_i \boldsymbol{V}_{,i} - \left(\widetilde{\underline{\underline{\boldsymbol{K}}}}_{ij} \boldsymbol{V}_{,j}\right)_{,i}$ is defined as the residual part of Eq. (2), and Ω denotes the volume of the computational domain. The Galerkin formulation for the compressible Navier–Stokes equations based on equal-order finite elements require a specific stabilization procedure [16]; the reader can refer to the review by Hughes et al. [13] on this topic. To fix this well-identified problem, a stabilization term is added to the weighting functions. Namely, the vector $\boldsymbol{W}$ is replaced by $\boldsymbol{W} + \underline{\underline{\boldsymbol{\tau}}}\mathcal{L}(\boldsymbol{W})$, where $\mathcal{L} \equiv \widetilde{\underline{\underline{\boldsymbol{A}}}}_i \partial/\partial x_i - \left(\widetilde{\underline{\underline{\boldsymbol{K}}}}_{ij} \partial/\partial x_j\right)_{,i}$ is associated with the Navier–Stokes operator (see Eq. (2)), and $\underline{\underline{\boldsymbol{\tau}}}$ is a characteristic time-scale matrix based on the eigenvalues of $\widetilde{\underline{\underline{\boldsymbol{A}}}}_0$, $\widetilde{\underline{\underline{\boldsymbol{A}}}}_i$, and $\widetilde{\underline{\underline{\boldsymbol{K}}}}_{ij}$. Thus, the semidiscrete Galerkin least-squares formulation of Eq. (2) reads

$$\int_\Omega \left[\boldsymbol{W} + \underline{\underline{\boldsymbol{\tau}}}\mathcal{L}(\boldsymbol{W})\right] \cdot \left[\widetilde{\underline{\underline{\boldsymbol{A}}}}_0 \boldsymbol{V}_{,t} + \mathcal{L}(\boldsymbol{V})\right] \mathrm{d}\Omega = 0 \tag{4}$$

This stabilization procedure is defined locally through the matrix $\underline{\underline{\boldsymbol{\tau}}}$ on each element, corresponding to the addition of an artificial viscosity to also control flow regions dominated by convection. Moreover, the streamline upwind Petrov–Galerkin stabilization, in which the diffusion term is neglected in the weighting functions, is also implemented in the AETHER solver.

The space discretization is obtained by projecting Eq. (4) on the space of equal-order interpolation functions. These functions are noted N_a, where a indicates the associated node number. Lagrange polynomials are used, taking the value 1 at $\boldsymbol{x}_a$ and 0 otherwise, that is $N_a(\boldsymbol{x}_b) = \delta_{ab}$, where δ_{ab} stands for the Kronecker symbol. The polynomial order of the interpolation functions can be increased, as illustrated in Fig. 1 for a one-dimensional element, to increase the numerical order of the space discretization. It must also be observed that the resolution on triangular elements is of second order for O_1-interpolation functions.

The finite elements considered in this study are isoparametric, that is the same interpolation or shape functions are used to interpolate the space coordinates $\boldsymbol{x}$ and the unknown vector $\boldsymbol{V}$, and they are also symmetric. The Jacobian matrices involved in metric tensors can be easily calculated thanks to the two interpolation formulas

$$\boldsymbol{V} = \sum_a^{n_n} N_a(\boldsymbol{x}) \boldsymbol{V}_a \quad \text{and} \quad \boldsymbol{x} = \sum_a^{n_n} N_a(\boldsymbol{x}) \boldsymbol{x}_a$$

where n_n is the number of modes. These symmetrical elements have flat faces and nodes at equal distance from each others. An easier algorithmic implementation is then obtained because the Jacobian matrix is shared by all elements. The space differentiation is also straightforward inside the element. Another property induced by this formulation, and which will be used for implementing the filtering, is that a polynomial interpolation function in the reference element remains polynomial in the real element.

C. Variational Multiscale Approach for Large-Eddy Simulation

As mentioned in Sec. I, the Navier–Stokes equations are filtered in space for large-eddy simulation. This leads to the introduction of additional terms in the governing equations. These subgrid-scale terms represent the interactions with the missing scales and need to be modeled. Among all these terms, the velocity subgrid-scale tensor $\underline{\underline{\mathbb{T}_u}}$ is dominant [17–19], and consequently only this term is considered

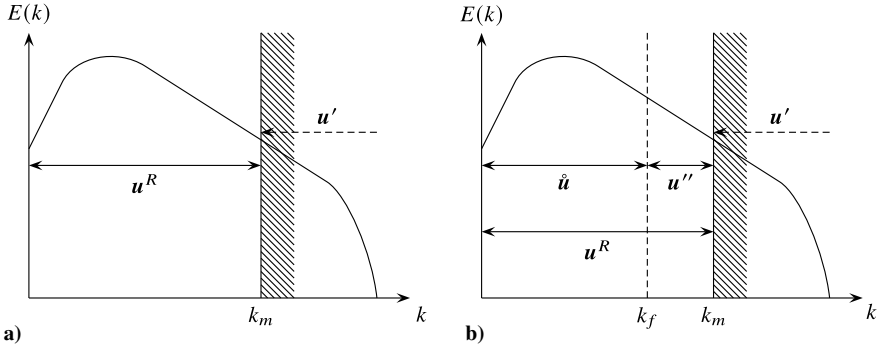

Fig. 2 Representations of a) classical LES approach, and b) separation of resolved scales for the VMS approach.

thereafter. If $\boldsymbol{U}^R$ denotes the unknown vector associated with resolved scales (see the sketch of the turbulent kinetic energy $E(k)$ in Fig. 2a, where k_m stands for the mesh cutoff wave number), the filtered Navier–Stokes equations are given by

$$\boldsymbol{U}^R_{,t} + \underline{\underline{\boldsymbol{A}}}^R_i \boldsymbol{U}^R_{,i} = \left(\underline{\underline{\boldsymbol{K}}}^R_{ij}(\nu, \boldsymbol{U}^R)\boldsymbol{U}^R_{,j}\right)_{,i} + \underline{\underline{\mathbb{T}_u}}$$

The standard closure for $\underline{\underline{\mathbb{T}_u}}$ is provided by the Smagorinsky model [17,19]. Dissipation effects are imposed through the introduction of a turbulent viscosity ν_t, and the tensor $\underline{\underline{\mathbb{T}_u}}$ is expressed from the deviatoric part $\underline{\underline{\boldsymbol{S}}}^D$ of the strain tensor as

$$\begin{cases} \underline{\underline{\mathbb{T}_u}} = \left(\underline{\underline{\boldsymbol{K}}}^R_{ij}\left(\nu_t, \boldsymbol{U}^R\right)\boldsymbol{U}^R_{,j}\right)_{,i} \\ \nu_t = (C_S\Delta_m)^2\sqrt{2\underline{\underline{\boldsymbol{S}}}^D(\boldsymbol{u}^R):\underline{\underline{\boldsymbol{S}}}^D(\boldsymbol{u}^R)} \end{cases} \tag{5}$$

where Δ_m is a characteristic scale of the element, and the colon denotes the matrix product. The nominal value of the Smagorinsky constant is taken to be $C_S = 0.18$, but this turbulence model is known to be very dissipative [19–21]. Several models such as the selective Smagorinsky model [21,22] and the dynamic Smagorinsky model [23] have brought improvements by decreasing the value of this artificial viscosity ν_t thanks to the local properties of the flow, without modifying the Laplacian functional form, and thus the large range of resolved scales affected by the subgrid-scale dissipation [24].

To overcome this difficulty, the variational multiscale approach has been retained by following the previous studies by Sagaut and Levasseur [8] and Levasseur et al. [9]. For this purpose, the resolved velocity field $\boldsymbol{u}^R$ is split into large $\mathring{\boldsymbol{u}}$ and small $\boldsymbol{u}''$ scales, as illustrated in Fig. 2b, where k_f is the filter cutoff wave number associated with the scale separation. An explicit filtering is here implemented to perform the scale separation; this point is developed in the next section. The key idea of such a model is to neglect the interactions between the larger resolved scales and the subgrid scales. Using the same formalism as in expression (5), the VMS formulation is then given by

$$\begin{cases} \underline{\underline{\mathbb{T}_u}} = \left(\underline{\underline{\boldsymbol{K}}}^R_{ij}(\nu_t, \boldsymbol{U}'')\boldsymbol{U}''_{,j}\right)_{,i} \\ \nu_t = (C_{\text{VMS}}\Delta_m)^2\sqrt{2\underline{\underline{\boldsymbol{S}}}^D(\boldsymbol{u}''):\underline{\underline{\boldsymbol{S}}}^D(\boldsymbol{u}'')} \\ C_{\text{VMS}}\Delta_m = C_S\Delta_f[(\Delta_f/\Delta_m)^{4/3} - 1]^{-3/4} \end{cases} \tag{6}$$

where the expression of the coefficient C_{VMS} can be determined by following the rationale introduced by Lilly [23] with the relevant range of scales, leading to the last relationship in system (6). The two length scales Δ_f and Δ_m are linked to the filter and the element, respectively. The mean length scale can be reasonably built on the cube root of its volume Ω^e as $\Delta_m = \sqrt[3]{\Omega^e}$. A macro-element of volume Ω^M, defined as the element built on each element sharing a common node, is also introduced, as illustrated in Fig. 3. The filter length scale is then computed as $\Delta_f = \sqrt[3]{\Omega^M}$. The use of these two

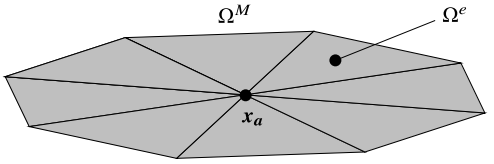

Fig. 3 Macro-element Ω^M used for the calculation of Δ_m at x_a.

volumes with $\Omega^e < \Omega^M$ allows to ensure that the coefficient C_{VMS} can always be determined over a given unstructured grid. Moreover, the VMS model is only active away from the wall where the mesh is unstructured but almost isotropic, hence the choice made here. The definition of the length scales Δ_m and Δ_f is not unique and is still discussed [10] in the literature.

Both formulations (5) and (6) are solved for the entropy variables introduced in the previous section; see Eq. (2). Accordingly, the general filtering Navier–Stokes equation is given by

$$\widetilde{\underline{\underline{\boldsymbol{A}}}}^R_0 \boldsymbol{V}^R_{,t} + \widetilde{\underline{\underline{\boldsymbol{A}}}}^R_i \boldsymbol{V}^R_{,i} = \left(\widetilde{\underline{\underline{\boldsymbol{K}}}}^R_{ij} \boldsymbol{V}^R_{,j}\right)_{,i} + \widetilde{\underline{\underline{\mathbb{T}_v}}}$$

where the tensor $\widetilde{\underline{\underline{\mathbb{T}_v}}}$ again involves subgrid-scale terms introduced by the filtering. The VMS approach (6) for entropy variables reads as

$$\begin{cases} \widetilde{\underline{\underline{\mathbb{T}_v}}} = \left(\widetilde{\underline{\underline{\boldsymbol{K}}}}^R_{ij}(\nu_t, \boldsymbol{V}'')\boldsymbol{V}''_{,j}\right)_{,i} \\ \nu_t = (C_{\text{VMS}}\Delta_m)^2\sqrt{2\underline{\underline{\boldsymbol{S}}}^D(\boldsymbol{V}''):\underline{\underline{\boldsymbol{S}}}^D(\boldsymbol{V}'')} \\ \boldsymbol{V}'' = \frac{1}{T^R}\left(T^R V_1^R, u_1'', u_2'', u_3'', -1\right)^T \end{cases} \tag{7}$$

The nonlinear change of variables leads to a particular expression of the subgrid terms in the primitive energy equation with respect to the Smagorinsky model.

D. Explicit Filtering Within Finite Element Method

The splitting of the resolved velocity field $\boldsymbol{u}^R$ into a low-wave-number component $\mathring{\boldsymbol{u}}$ and its complement $\boldsymbol{u}''$, as drawn in Fig. 2, is performed by introducing an explicit filtering procedure within the finite element method. Motivations for using an explicit filtering in LES and various numerical issues can be found in reviews [17,19,25], but the filtering procedure is almost exclusively developed for structured meshes. Nevertheless, Najafi-Yazdi et al. [26] have recently proposed the implementation of compact discrete filters on unstructured two-dimensional grids. In order not to affect too much the efficiency of the finite element algorithm, the filtering is here achieved by considering embedded piecewise polynomials. Brazell et al. [27] have proposed a similar approach to implement the dynamic Smagorinsky model within the discontinuous Galerkin method. The local solution determined with O_i functions (see Fig. 1) is interpolated at a lower order using O_{i-1} polynomials, as illustrated in Fig. 4. For a solution obtained at order O_3, the resolved field $\boldsymbol{u}^R$ is described with O_2 interpolation functions and the filtered field $\mathring{\boldsymbol{u}}$ with O_1 interpolation functions. More

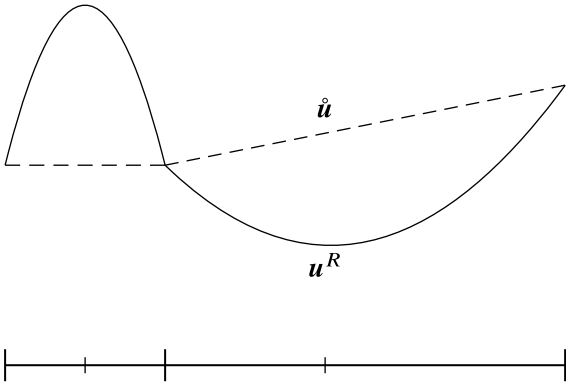

Fig. 4 Filtering of a quadratic solution u^R in solid line using linear interpolation functions.

generally, the filtering order is $O_f = O_m - O_{\text{if}}$, where O_m is the order of the Navier–Stokes simulation, and O_{if} is the order of the interpolation functions used to calculate the filtered field. A robust numerical approach is thus obtained, with a reasonable computational cost, and the increase of the order of the Navier–Stokes simulation is associated with that of the filtering procedure.

E. Hybrid Variational Multiscale Reynolds-Averaged Navier–Stokes Formulation

The two LES models provided by Eqs. (5) and (6) are implemented through a DES-like approach [1,28,29] in the solver. The DDES model of Spalart et al. [4] based on the Spalart–Allmaras (S-A) turbulence model is here solved in the near-wall region of the attached boundary layer, and a large-eddy simulation is performed elsewhere. In the original model, the transition between the two zones is driven by the f_d function

$$\begin{cases} f_d = 1 - \tanh[(8r_d)^3] \\ r_d = \dfrac{\nu_t + \nu}{\sqrt{u^R_{i,j}u^R_{j,i}}(\kappa d)^2} \end{cases} \tag{8}$$

where d is the distance to the wall, and κ is the von Kármán constant in the logarithmic law. The DDES model reduces to the S-A model in the region where $f_d \to 0$, whereas a large-eddy simulation provided by the DDES model is performed in the region where $f_d \to 1$. This function has been slightly adapted in the present study to introduce the VMS model, which will replace the DDES model in the region $f_d \to 1$. The modified transition function f_c is given by

$$f_c = \begin{cases} 0 & \text{if } f_d < \alpha_i \\ \dfrac{f_d - \alpha_i}{\alpha_s - \alpha_i} & \text{if } f_d \in [\alpha_i, \alpha_s] \\ 1 & \text{if } f_d > \alpha_s \end{cases}$$

where the values of the coefficients α_s and α_i must be taken in the interval [0, 1], with $\alpha_s > \alpha_i$. The numerical values have been set to $\alpha_s = 0.9$ and $\alpha_i = 0.5$ in this study. In that way, the application of the S-A model is enforced near the wall, but a full VMS model is applied before the edge of the boundary layer. This transition function f_c is applied to the turbulent viscosity ν_t, to the filtered velocity field $\boldsymbol{u}''$, and to the gradient of the entropy variables $\partial \boldsymbol{V}''/\partial \boldsymbol{x}$. The transition has been chosen linear for an easier implementation. At each node $\boldsymbol{x}_a$ of the mesh, the hybrid variables used as input in the VMS formulation (7) are thus calculated with the following relationships:

$$\begin{cases} \boldsymbol{u}''|_{\text{hyb}} = (1 - f_c)\boldsymbol{u}^R + f_c\boldsymbol{u}'' \\ \left.\dfrac{\partial \boldsymbol{V}''}{\partial \boldsymbol{x}}\right|_{\text{hyb}} = (1 - f_c)\dfrac{\partial \boldsymbol{V}^R}{\partial \boldsymbol{x}} + f_c\dfrac{\partial \boldsymbol{V}''}{\partial \boldsymbol{x}} \\ \nu_t|_{\text{hyb}} = (1 - f_c)\nu_t^{\text{DDES}} + f_c\nu_t^{\text{VMS}} \end{cases} \tag{9}$$

III. Taylor–Green Vortices

The Taylor–Green vortices provide an academic framework to study dissipation mechanisms involved in LES, as proposed by Fauconnier [30], among others. The homogeneous flow slowly turns to be turbulent by reaching a peak of dissipation; a complete description can be found in Brachet et al. [31]. The DNS solution of Fauconnier [30] is used as a reference solution here. The present simulations are performed with the compressible AETHER solver. This is, however, not an issue with respect to the moderate Mach number of the simulation, $M = u_0/c_0 \leq 0.3$. This flow becomes turbulent for a Reynolds number $Re_{L_0} = u_0L_0\rho_0/\mu$ higher than 500, where L_0 defines the size of the box, namely $\Omega = 2\pi L_0 \times 2\pi L_0 \times 2\pi L_0$. The Reynolds number is chosen to be 1500 and corresponds to the value of the DNS [30]. Accordingly, the minimal number of points in each direction to correctly solve the turbulent flow is $N = 256$, and the time step is $\Delta t = 5 \times 10^{-3}$ s. Two structured meshes based on O_3 finite element are used on a same box of length 2π m (i.e., $L_0 = 1$ m). The first mesh is the DNS mesh used to compare AETHER DNS results with the numerical results by Fauconnier [30]. The second mesh is the LES mesh with $N = 64$ points per direction.

Two quantities are more particularly examined: the dissipation and the kinetic energy. They are made dimensionless by the quantities $t_c = L_0/u_0$ for the time t, u_0^2 for the kinetic energy K, and u_0^2/t_c for the dissipation. The kinetic energy K is calculated in the volume as

$$K = \frac{1}{\rho_0\Omega}\int_\Omega \rho\frac{\boldsymbol{u}\cdot\boldsymbol{u}}{2}\,\mathrm{d}\Omega$$

whereas the dissipation is defined as $\epsilon^T = -\partial K/\partial t$ in the present case. This total dissipation can be split into three different contributions. The first component is the resolved dissipation ϵ^R determined from the LES-resolved scales

$$\epsilon^R = \frac{2\nu}{\rho_0\Omega}\int_\Omega \rho\underline{\underline{\boldsymbol{S}}}^D(\boldsymbol{u}^R):\underline{\underline{\boldsymbol{S}}}^D(\boldsymbol{u}^R)\,\mathrm{d}\Omega \tag{10}$$

The second dissipation ϵ'' is associated with the subgrid-scale model and is computed as

$$\epsilon''(\boldsymbol{u}'') = \frac{2}{\rho_0\Omega}\int_\Omega \rho\nu_t(\boldsymbol{u}'')\underline{\underline{\boldsymbol{S}}}^D(\boldsymbol{u}''):\underline{\underline{\boldsymbol{S}}}^D(\boldsymbol{u}'')\,\mathrm{d}\Omega \tag{11}$$

for the VMS model and $\epsilon''(\boldsymbol{u}^R)$ for the Smagorinsky model. In an ideal LES simulation, ϵ'' is the strict complement of ϵ^R to obtain ϵ^T. Unfortunately, stabilization and numerical errors are also introduced. This last implicit contribution denoted ϵ^N can be obtained by considering the balance equation $\epsilon^T = \epsilon^R + \epsilon'' + \epsilon^N$ and is expected to be small for a DNS.

The time evolutions of K and ϵ^T are plotted in Fig. 5. At the beginning, turbulent structures consist of large vortices with a weak dissipation rate. From $t = 2$, these large structures start to break into smaller ones, and an energy transfer from larger scales to smaller scales occurs. The kinetic energy begins to fall, and the dissipation increases accordingly. Three snapshots of the turbulent flow based on the λ_2 criterion [32] are displayed in Fig. 6. The transition to turbulence is clearly visible between Figs. 6a and 6b. As expected, the dissipation is basically imposed by the larger scales of the flow, reaching a maximum at $t = 9$, as shown in Fig. 6b. A full energy cascade is then observed, and the flow motion is finally stopped by the molecular dissipation effects. It has been checked that ϵ^T takes values very close to ϵ^R, and a good comparison is found with the DNS by Fauconnier [30], as displayed in Fig. 5.

Three LES results are reported here, performed on the LES grid with the numerical parameters provided in Table 1. Various other results have been obtained [33] but are not shown here. The turbulent kinetic energy spectrum is plotted in Fig. 7 for the three models A, C, and E. The VMS and Smagorinsky models follow the DNS results up to the mesh cutoff wave number $k/k_{\max} = 64/254 \simeq 0.25$. The resolution of the low-wave-number components are imposed by the

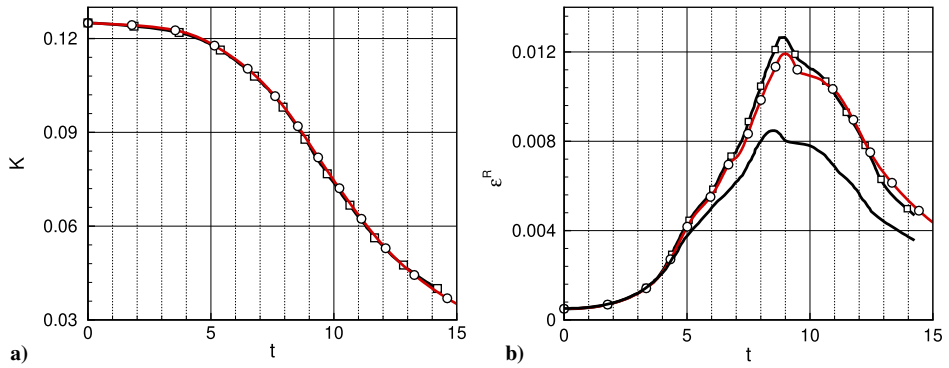

Fig. 5 Time evolution of a) kinetic energy, and b) total dissipation: Fauconnier's DNS (squares), AETHER's DNS (circles), and Fauconnier's DNS projected on the LES grid (solid line).

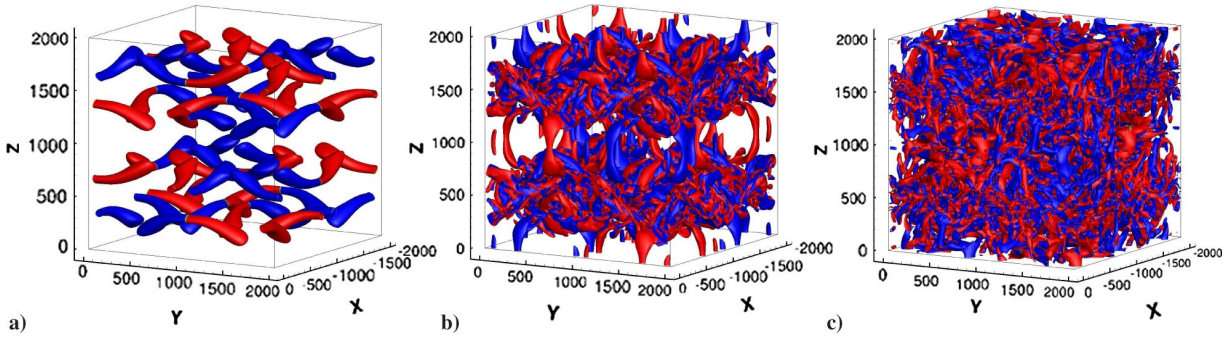

Fig. 6 DNS results at a) $t = 2$, b) $t = 9$, and c) $t = 15$. Vortical structures are shown using the λ_2 criterion for the value of $0.4 \times L_0/u_0$ colored by the vorticity in the z direction.

spatial domain size. The VMS model is able to correctly preserve the energy cascade occurring in the wave-number range $k/k_{\max} \in [0.04, 0.6]$, without creating energy pile-up near the cutoff wave number [21]. Moreover, the flow is not fully isotropic, leading to a spectral slope diverging from the classical $-5/3$.

The time evolution of the resolved dissipation ϵ^R (refer to Eq. (10)) is plotted in Fig. 8 for the three LES. The subgrid-scale dissipation ϵ'' (see Eq. (11)) has been added in dotted lines for VMS models. The dissipation (A) of the filtered DNS has a lower peak compare to the full DNS (see Fig. 5b) because smallest structures have been removed on the LES grid. The Smagorinsky model (C) deviates at $t = 5$ from the DNS result and provides the lowest level for the resolved dissipation. Large structures that generate the energy cascade and impose the dissipation rate are affected too much by the Smagorinsky model. This interpretation is confirmed by examining the two quantities ϵ^R and ϵ''. Both curves have the same shape but are different in level, which is expected because ϵ'' differs from ϵ^R only by the scalar ν_t, which is also computed from the resolved field. These results are slightly improved by the dynamic Smagorinsky model.

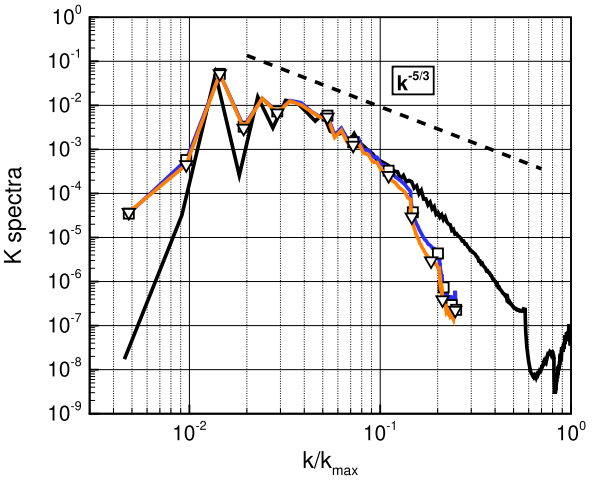

Fig. 7 Kinetic energy spectrum at $t = 10$ for AETHER DNS (squares), Smagorinsky model (C) (triangles), and VMS model (E) (diamonds).

Table 1 Captions associated with the different displayed results

Case	Description	Symbol
A	DNS results of Fauconnier, filtered on the LES mesh [30]	Solid line
B	LES with dynamic Smagorinsky model (Fourier space) [30]	Diamond
C	Present LES, Smagorinsky model, finite element O_3, Eq. (5)	Square
D	Present LES, VMS model, finite element O_3, Gaussian filter (order 2), Eq. (7)	Circle
E	Present LES, VMS model, finite element O_3, interpolation filtering (order 1), Eq. (7)	Triangle

For completeness, results obtained from two filtering procedures have been reported. The VMS model (D) is based on a Gaussian filter [9] and succeeds to accurately recover the resolved dissipation. A global inversion of the filtering matrix leads to a well-resolved filtered solution, inducing a high numerical cost here because no mass lumping is performed. The VMS subgrid-scale dissipation ϵ'' is 100 times lower than the value obtained with the Smagorinsky model. Its dynamics strictly follows the time events of the Taylor–Green vortices described by Brachet et al. [31] and retrieved by Fauconnier [30]. The model stands still to zero until $t = 7$. The vortex flow then becomes heavily distorted, corresponding to a full turbulent flow and the activation of the model. The second event occurs around $t = 8$, when the flow breakdown begins, up to the dissipation peak at $t = 9$.

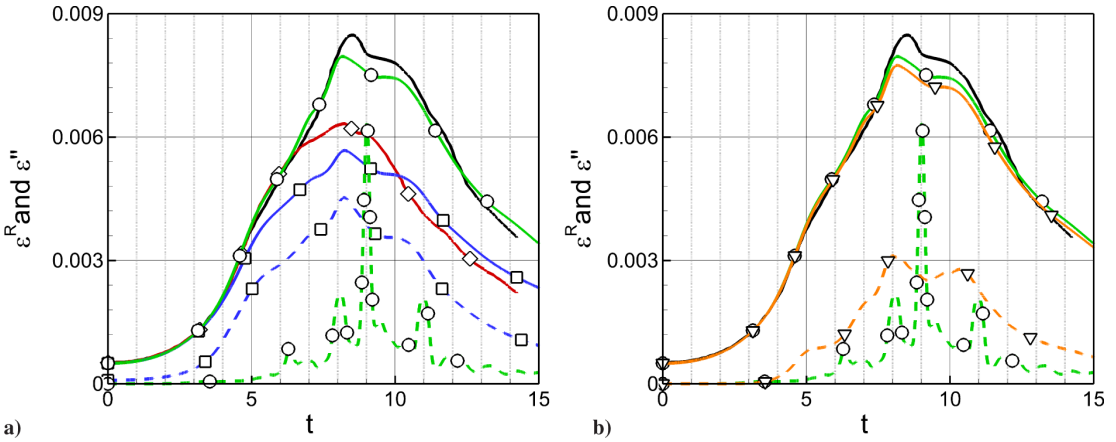

Fig. 8 Resolved (solid line) and subgrid-scale dissipation (dashed line): a) A, B, C, D models; and b) A, D, E models (refer to Table 1). Dissipation ϵ'' multiplied by a factor 100 for VMS (D) and 10 for VMS (E).

The second VMS model (E) is based on the new interpolation filtering introduced in the previous section and provides satisfying predictions. The subgrid-scale dissipation is lower than VMS model D, but much better than other models. The difference between the two VMS models can be observed with the time evolution of the dissipation. VMS model D involves a second-order filter, whereas VMS model E involves a first-order filtering to meet industrial requirements, with a computational cost 20 times lower. The flatter evolution obtained with VMS model E is clearly induced by the simplification of the filtering method. Despite this deteriorated performance of the filtering, VMS model E is retained to evaluate the near-wall treatment in the next section. The formulation indeed represents a good compromise between computing efficiency and accuracy.

IV. Noise of a Three-Element High-Lift Airfoil

The LEISA-2 problem has been introduced by Manoha and Pott-Pollenske [11] in the framework of the benchmark for airframe noise computation (BANC), available to the aeroacoustic community [34]. The slat-wing flat system is shown in Fig. 9 with a stowed chord of $C = 300$ mm, obtained when the slat and the flat are retracted in cruise condition. The slat chord is $C_s = 55.8$ mm, and the deflection angle is 27.834 deg. This high-lift configuration model comes from the original FNG Airbus geometry and corresponds to one of the smallest models built in the literature for experimental studies. The database was obtained from measurements performed in two facilities. The model was first mounted by DLR, German Aerospace Center in the F2 closed-section wind tunnel located in ONERA Le Fauga for aerodynamic investigations, whereas the acoustic measurements were achieved in the Acoustic Windtunnel Braunschweig (AWB) anechoic open-jet wind tunnel at DLR Braunschweig. The database includes particle image velocimetry, laser Doppler velocimetry, and two-point correlations of the turbulent velocity field as well as wall pressure and radiated acoustic field spectra for comparison.

An insightful review on airframe noise is provided by Dobrzynski [35]. The present study focuses on the flow around the slat, identified as the dominant noise source, and aims at demonstrating that the VMS model (7) implemented in the hybrid DDES formulation (9) is able to reproduce the various physical phenomena encountered in such a configuration. An overview on similar geometries can be found in the numerical studies by Choudhari and Khorrami [36], Reuß et al. [37], Deck and Laraufie [38], Terracol et al. [39], and more recently Zhang et al. [40]. The laminar boundary layer developing near the cusp, that is the slat lower trailing edge, gives rise to the shear layer (1) generated in the slate-cove region, as illustrated in Fig. 10. Kelvin–Helmholtz instabilities (point 1-a) develop before vortex pairing and nonlinear interactions produce coherent turbulent structures. Their impingements on the slat inner part of the suction side (point 1-c) generate a strong impact noise (point 1-d) and tones through an aeroacoustic feedback loop. The latter appear to be an artifact of the model due to its moderate Reynolds number compared with those of the full scale geometry. Furthermore, this noise mechanism is significantly affected by the angle of attack and the freestream Mach number. The turbulent boundary layer develops along the slat suction side, leading to von Kármán vortices (point 2) after separation from the slat trailing edge. This wake flow is also disrupted by the turbulent bursts resulting from the shear-layer impingement (point 2-a).

A. Numerical Parameters

The two-dimensional LEISA-2 profile displayed in Fig. 9 has been extruded along the y axis from $y = 0$ mm to $y = 60$ mm. Periodic conditions are applied in the spanwise direction. The size of the computational domain is expected to contain at least two integral length scales. This was verified a posteriori in the present simulations. The inflow conditions [11] are the pressure $P_0 = 100{,}136$ Pa,

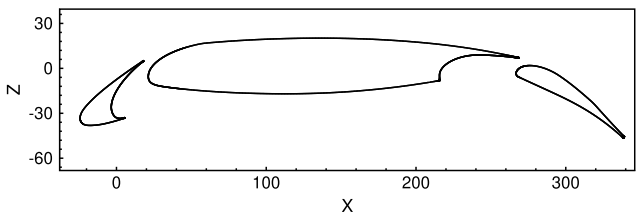

Fig. 9 Cross-sectional view of the LEISA2 (F16) high-lift wing.

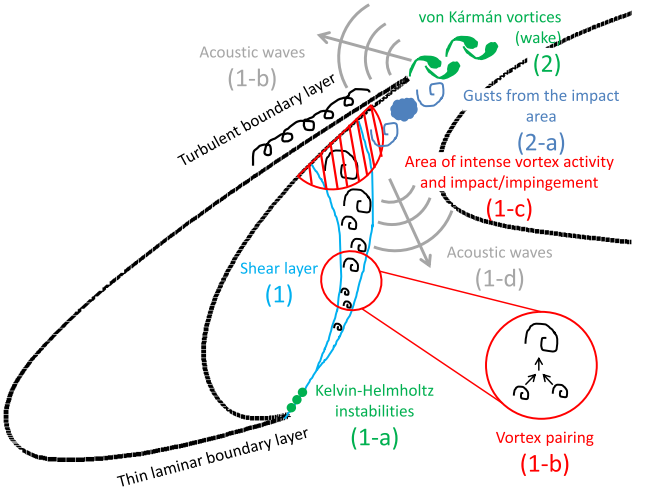

Fig. 10 Expected physical phenomena in the slat region.

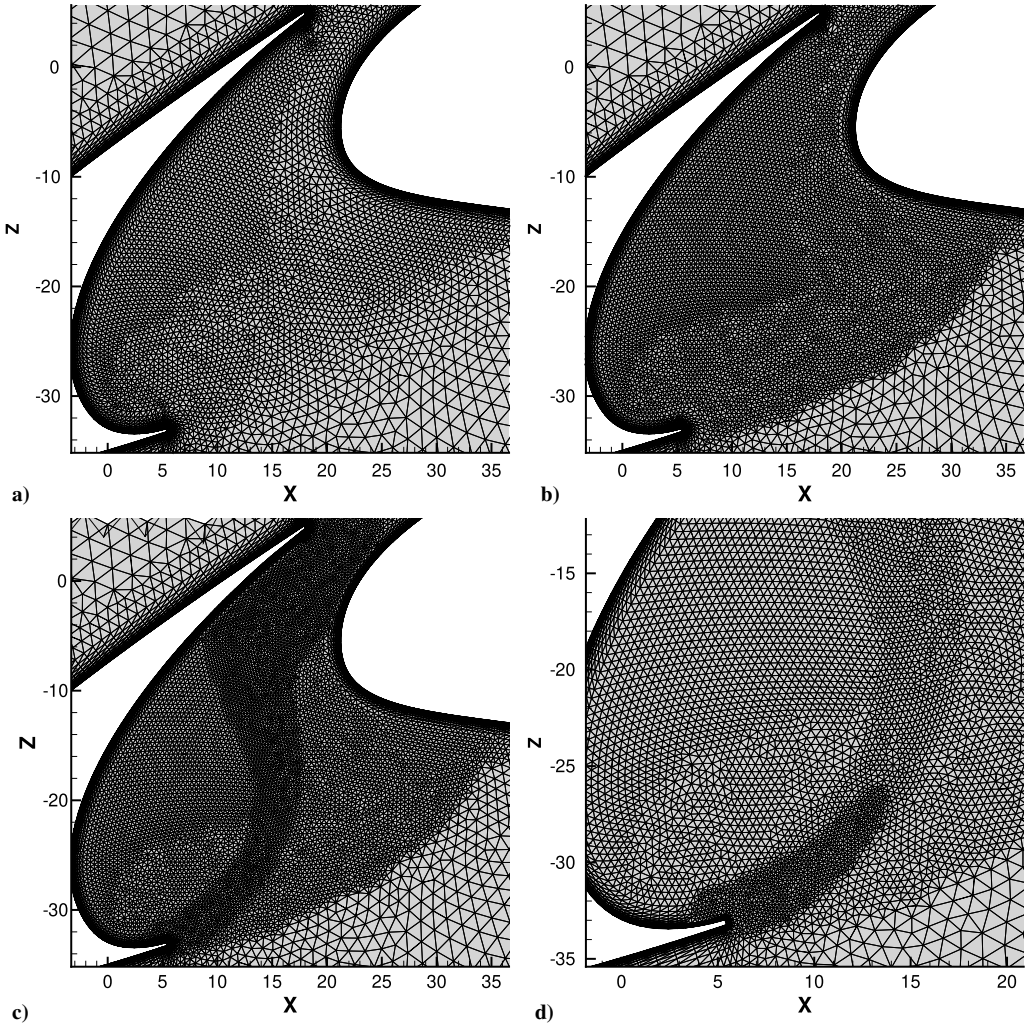

Fig. 11 Mesh building steps near the slat region: a) initial mesh, b) isotropic homogenization, c) refinement in the shear layer, and d) refinement near the slat trailing edge.

the freestream Mach number $M_\infty = 0.1804$, the temperature $T_0 = 289.45$ K, and the angle of attack $\alpha = 6.15$ deg. The Reynolds number based on the stowed chord is $Re = Cu_\infty/\nu \simeq 1.2 \times 10^6$, where $u_\infty = M_\infty \times c_0$ is the freestream velocity, and c_0 is the speed of sound. The Reynolds number based on the slat chord C_s is, however, more relevant for the slat region, $Re_s \simeq 2.5 \times 10^5$. The developing boundary layer around the slat leading edge is thus initially laminar.

To keep a reasonable mesh size, the flow around the slat is privileged in terms of node density. One of the main goals of the present study is indeed to demonstrate that the present hybrid model is able to describe the physical aeroacoustic mechanism involved in the slat cove, which has been identified as the dominant noise source [36]. The grid in the transverse direction is regular with a step size of $\Delta y = 0.5$ mm. In the x and z axes, the mesh is fully unstructured. The tetrahedral elements of order 3, corresponding to a spatial quadratic interpolation, have been selected. Three areas with distinct mesh sizes have been defined, as shown in Fig. 11. The first area is designed to have an average length scale of $\Delta x = \Delta z = 0.2$ mm. The second area following the shear flow between the slat and the main wing is designed to satisfy an average length scale of $\Delta x = \Delta z = 0.15$ mm. The third area located around the trailing edge of the slat lower part, the so-called cusp, has an average scale of $\Delta x = \Delta z = 0.1$ mm. The resulting grid is made of $n_n = 35 \times 10^6$ nodes and 26×10^6 elements. The mesh properties are summarized in Table 2, where the subscript "ref" corresponds to the area of interest between the slat and the wing, Δx^i_{ref} is the mean length scale in a transverse plane of the ith subarea described previously, Δy_{ref} is the length scale along the y axis, and $\Delta n_{\min}$ is the distance of the closest point from the wall. The time step is taken equal to 7.0×10^{-7} s, corresponding to a Courant-Friedrichs-Lewy (CFL) number of $(U_\infty + c_0)\Delta t/\Delta_m \simeq 2.8$ around the slat cusp.

The simulation is performed with the AETHER code and the hybrid VMS method (7) including the interpolation filtering, whereas the near-wall flow is computed with a DDES-like procedure according to the hybrid formulation (9). A RANS simulation based on the Spalart–Allmaras turbulence model is first carried out to initialize the VMS computation. The large-eddy simulation is then performed during 12.5 convected times C/u_∞ so that the transient regime leaves the computational domain. The data are then recorded during 125 ms corresponding to roughly 25 convected times.

Finally, four other large-eddy simulations have been performed, but they are not directly reported here [33]. All these additional simulations are based on the selective Smagorinsky model combined

Table 2 Properties of the final mesh for the LEISA-2 benchmark

$n_n \times 10^6$	O_i	$\Delta x^1_{\text{ref}}\ C \times 10^{-4}$	$\Delta x^2_{\text{ref}}\ C \times 10^{-4}$	$\Delta x^3_{\text{ref}}\ C \times 10^{-4}$	$\Delta y_{\text{ref}}\ C \times 10^{-4}$	$\Delta n_{\min}\ C \times 10^{-4}$
35	3	6.66	5.00	3.33	16.66	0.05

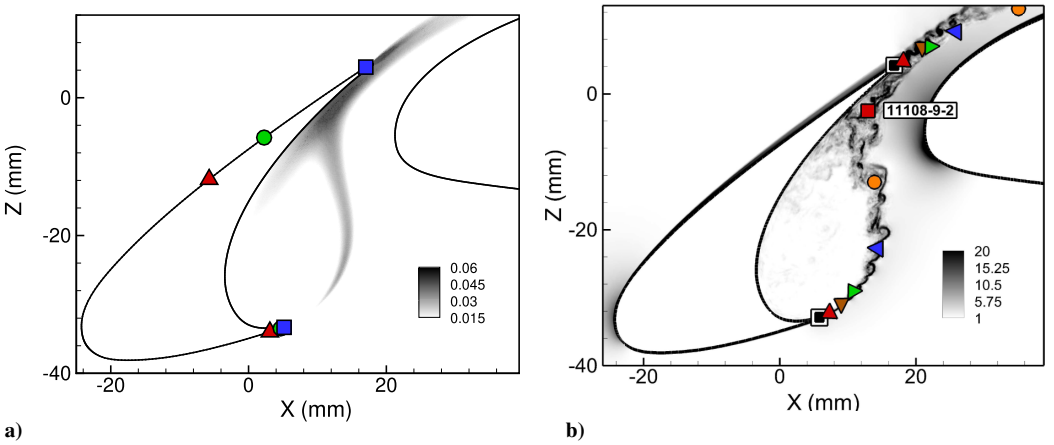

Fig. 12 Representations of a) dimensionless turbulent kinetic energy, and b) instantaneous schlierenlike view (arbitrarily units).

with the DDES approach, except that the turbulent viscosity is based on the magnitude of the local vorticity through the rotation rate tensor. The first two are performed on the same grid (see Table 2), with a spatial order O_2 and O_3, and the two others are performed with a spatial order O_2 for the interpolation functions, but with a grid made of $n_n = 38 \times 10^6$ and $n_n = 89 \times 10^6$ nodes, respectively.

B. Overview of the Turbulent Flow

The dimensionless turbulent kinetic energy $k_t = (\overline{u^{*2}} + \overline{v^{*2}} + \overline{w^{*2}})/(2u_\infty^2)$ is plotted in Fig. 12a, where $\boldsymbol{u}^*$ denotes the fluctuating velocity field. The turbulent activity is concentrated along the shear layer, and the turbulent kinetic energy reaches its maximum around the impact area with a value $k_t \simeq 0.06$. The recirculating flow that occurs inside of the slat cavity can also be clearly identified. A schlierenlike view obtained by computing the norm of the density gradient $\|\nabla\rho\|/2$ is shown in Fig. 12b to illustrate the turbulent flow development. On the early stage of the shear layer, the generation of Kelvin–Helmholtz vortices is observed. These coherent structures are convected until a breakdown occurs. The view appears to be more blurry, meaning that smaller structures are generated through the energy cascade. These structures are partly dragged in the cavity recirculation, whereas the main part is sucked by the wake. Moreover, von Kármán structures can be observed in the wake.

To illustrate the improvement made by the VMS model, the longitudinal velocity gradient $\partial u/\partial x$ used as input in the strain tensor $\underline{\underline{S}}^D$ for LES models is now examined. The results obtained with the DDES Smagorinsky model on the same grid are also considered for comparison. Both fields have been normalized with u_∞/C and are displayed in Fig. 13. The DDES Smagorinsky model is activated not only in the whole recirculating turbulent flow but also in the outer area of the cavity slat, as indicated by the large spots around the leading edge of the main wing in Fig. 13a. On the contrary, the explicit filtering introduced by the VMS model (7) to feed the strain tensor, which finally determines the value taken by the turbulent viscosity, enables the selection of the thinner resolved structures, as shown in Fig. 13b. The regions where the viscosity model needs to be applied are thus better identified.

C. Near-Wall Flow

The computed static pressure distribution is plotted in Fig. 14 and is compared to the reference measurements (F2-ONERA). The flow is found to be attached along the slat-wing flat airfoil. The wall pressure coefficient is well predicted except along the slat extrados, where the simulation provides overestimated values. This discrepancy, however, must be put in perspective with installation effects. The reference angle of attack α has been slightly adjusted in the different wind tunnels to recover the same flow regime. Additional RANS simulations [33] have shown that the experimental C_p distribution is recovered for a value of the angle of attack of $\alpha \simeq 5.85$ deg. The reference value of α is kept for this study in agreement with the benchmark [11].

The boundary layer presents distinct evolutions around the slat, with a thicker boundary layer along the extrados; refer to Fig. 13. Mean wall-normal velocity profiles have been reported in Fig. 15 in wall units, for three positions along the intrados near the slat cusp in solid line and three positions along the extrados near the slat trailing edge in dashed line. The probe positions are provided in Fig. 12a. Thanks to the mean pressure gradient induced by the airfoil curvature, a thinner laminar boundary layer develops along the bottom part of the slat. The turbulent Reynolds number is about $Re_\tau = u_\tau\delta/\nu \simeq 50$, and the turbulent viscosity is never greater than one fourth of the

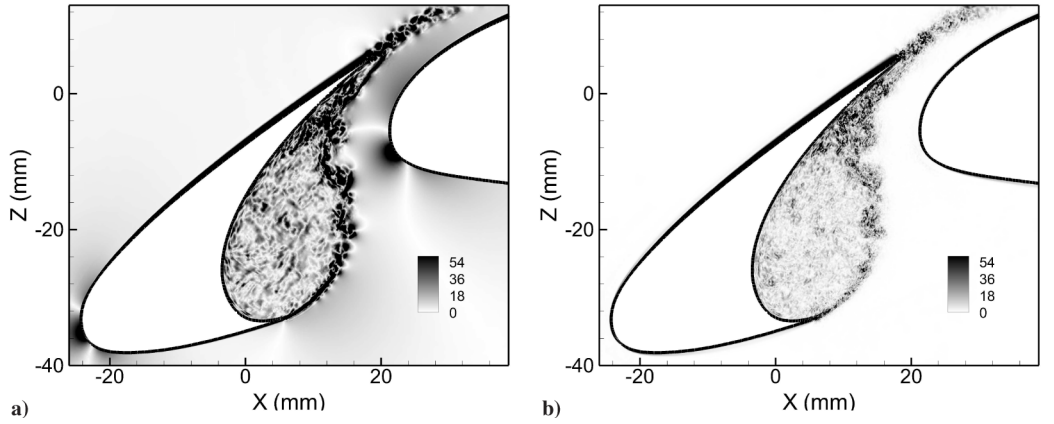

Fig. 13 Representations of a) snapshot of dimensionless $\partial u^R/\partial x$ used as input in the DDES Smagorinsky model, and b) snapshot of dimensionless $\partial u''/\partial x$ for the VMS model.

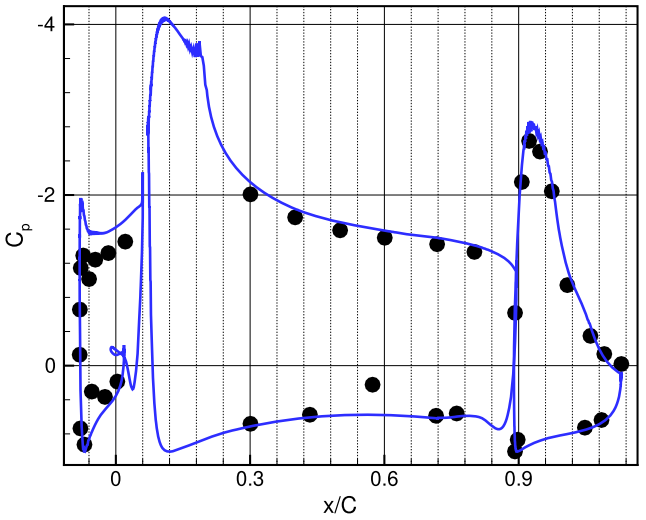

Fig. 14 Computed wall pressure coefficient around the three-element airfoil in solid line; symbols stand for experimental data [11].

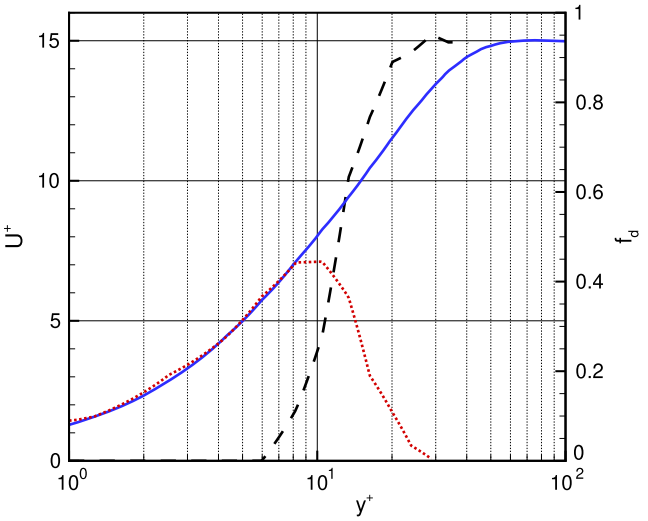

Fig. 16 Behavior of the hybrid method near the wall at position 2 at the slat intrados: transition function f_d (dashed line), $\overline{u^{R+}}$ (solid line), and hybrid mean velocity $\bar{u}^+|_{\text{hyb}}$ (dotted line).

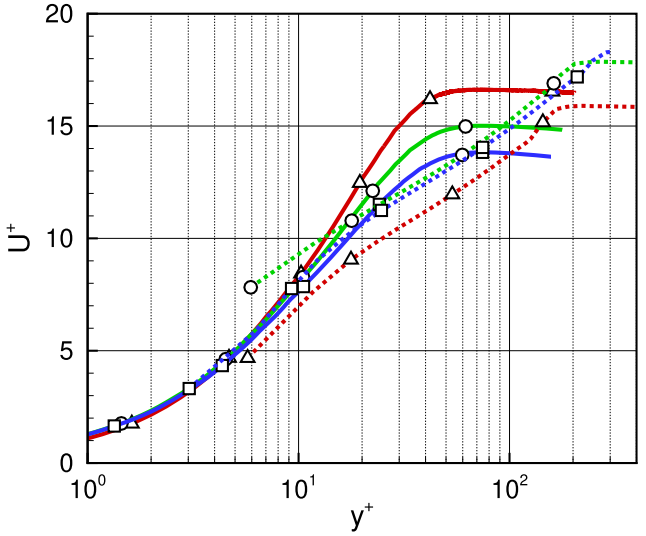

Fig. 15 Transverse mean velocity profiles: positions 1 (triangles, solid line), 2 (circles, solid line), and 3 (squares, solid line) along the intrados; positions 1 (triangles, dashed line), 2 (circles, dashed line), and 3 (squares, dashed line) along the extrados.

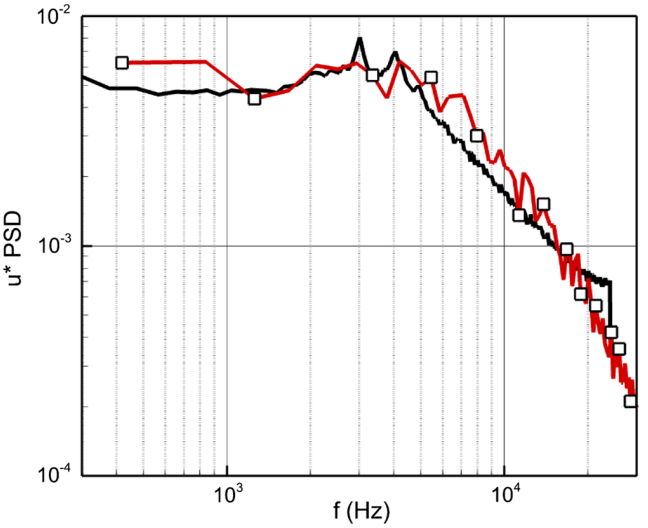

Fig. 17 PSD of the longitudinal fluctuating velocity at probe 11108-9-2: LES-VMS (squares), and measurements (F2-ONERA).

molecular one in this region. On the contrary, a beginning of the boundary-layer transition occurs on the upper side through the DDES-VMS hybrid approach. The Reynolds number is around $Re_\tau \simeq 250$ in this area, and an early stage of logarithmic region might be observed in the velocity profiles. A transition prediction of the boundary layers has been performed using the code 3C3D developed by Perraud et al. [41] at ONERA, and both slat boundary layers are found to be laminar.

The behavior of the hybrid model Eq. (9) is illustrated in Fig. 16, with the transverse mean velocity profile of the boundary layer $\overline{u^{R+}}$ at the slat intrados represented in the solid line. This velocity is composed of the RANS solution from the wall up to the interface with the VMS-LES region, defined by the transition function f_d in dashed line (refer to Eq. (8)) and of the average of the VMS solution in the higher part. The production region of the boundary layer is located in the resolved region of the large-eddy simulation, which ensures a correct development of the turbulent flow.

D. Velocity Spectra

The turbulence development has been examined from the trailing edge of the slat cusp inside the cavity; refer to Fig. 12b. With the effective angle of attack being slightly higher for the simulation than for experiments, as already discussed with the mean pressure distribution in the previous section, this misalignment leads difficulties for the interpretation. Nevertheless, the computed spectrum of the longitudinal velocity fluctuation is compared with hot-wire measurements in Fig. 17 for probe 11108-9-2 located near the impingement. An excellent agreement is found, indicating that the developing shear layer is well reproduced by the VMS model.

Numerical power spectral densities (PSDs) are calculated with the periodogram algorithm using 50 blocks without overlap. The time history of the velocity spectrum along the shear layer is provided in Fig. 18; the symbols correspond to the probe position along the shear layer displayed in Fig. 12b. For the first positions near the cusp, the PSD of the velocity is dominated by a peak associated with Kelvin–Helmholtz structures. The peak frequency can be estimated from the relationship $f_{\text{KH}} = 0.033 u_m/\delta_\theta$, where δ_θ is the momentum thickness, and u_m is the mean velocity of the shear layer. From the properties of the mean velocity profile in the shear layer [33], one obtains $f_{\text{KH}} \simeq 30$ kHz. The convective development of the transitional shear layer is reflected in the decrease of the peak associated with the momentum thickness growth and by the broadband feature of spectra. The Reynolds number is, however, not high enough to observe the

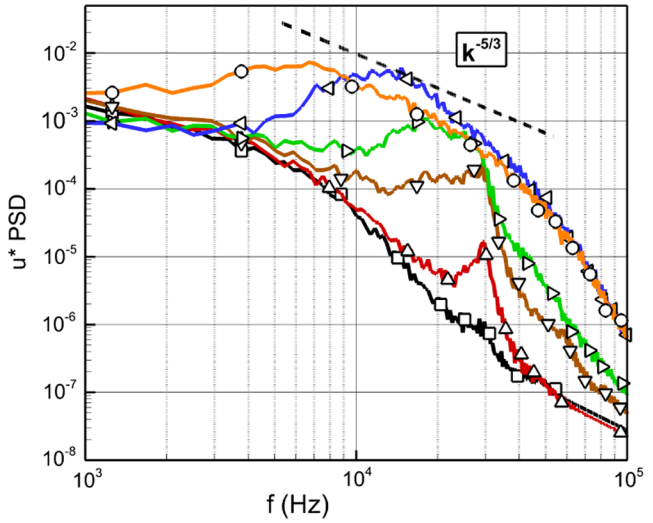

Fig. 18 Evolution of the longitudinal velocity spectrum along the shear layer (refer to Fig. 12b for symbols).

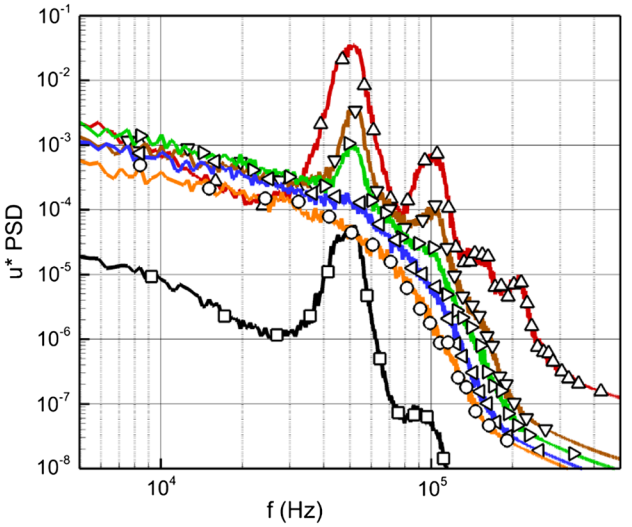

Fig. 19 Evolution of the longitudinal velocity spectrum along the slat wake (refer to Fig. 12b for symbols).

$-5/3$ slope of isotropic turbulence. Last, no tone is observed in the present simulation with respect to the selected angle of attack and the spanwise length of the computational domain. Tones could be generated by resonances in the slat cave. As in a cavity, the physical mechanism can be interpreted as Rossiter-like modes. The reader can refer to the study by Terracol et al. [39] for a complete discussion on this topic.

The evolution of the velocity spectra in the slat wake is plotted in Fig. 19. The first probe, corresponding to square symbols, is located inside the boundary layer just before the trailing edge, as shown in Fig. 12b, and the turbulence intensity is weak at this location. Spectra are marked by several bumps developing along the wake flow. The fundamental frequency is associated with the vortex shedding occurring at the slat trailing edge [42,43]. The von Kármán frequency can be estimated from the Strouhal number $St = f_s l/u_\infty = 0.2$ based on the trailing edge thickness $l = 0.25$ mm, which yields $f_s \simeq 50$ kHz. At least the three first harmonics of this frequency can be observed in velocity spectra. The wake flow appears to be transitional, in agreement with the moderate Reynolds number based on the slat chord Re_s, and is also perturbed by the shear-layer impingement inside the cove slat, generating turbulent bursts. That can also be explained by the unusual enlargement of the peaks mentioned previously. Both flows finally merge near the slat trailing edge.

E. Radiated Acoustic Field

An overview of the radiated acoustic field is shown in Fig. 20, with a snapshot of the divergence of the fluctuating velocity. Three distinct noise components can be observed in the slat region. They are associated with the vortex shedding at the slat trailing edge, with the shear-layer impingement inside the slat cove at a lower frequency, and with the interaction of the slat wake with the main body at a higher frequency. Moreover, as already mentioned in a previous section dealing with the static pressure distribution, the flow remains attached along the three-body system.

Two methods have been used to determine the radiated pressure, linked to the possibilities offered by the solver. Both approaches are based on the Curle formulation [44], in which only the fluctuating wall pressure term is considered as input data; refer to Eq. (12). The integration is performed over the three surfaces of the high-light wing. In the first method, the computed wall pressure is stored every 25 time steps, and the PSD of the radiated pressure field is then determined for an observer located at a distance $r = 1$ m and an angle $\theta = -90$ deg, that is below the three-body airfoil. The result is plotted in dashed line in Fig. 21. In the second method valid for compact surfaces only, the variation of the retarded time in Curle's integral is assumed to be negligible. The lift coefficient C_L stored at each time step by default in the solver can then be used in the integral formulation to estimate the acoustic far-field spectrum

$$p'(\boldsymbol{x},t) = \frac{1}{4\pi r c_0}\int_S \frac{\boldsymbol{r}\cdot\boldsymbol{n}}{r}\frac{\partial p(\boldsymbol{y},\tau)}{\partial t}\,\mathrm{d}\boldsymbol{y} \simeq \frac{\rho_\infty U_\infty^2}{4\pi r c_0}\frac{\partial C_L}{\partial t} \tag{12}$$

where $\boldsymbol{r} = \boldsymbol{x} - \boldsymbol{y}$ is the separation vector, $\boldsymbol{n}$ is the outward normal vector, and $\tau = t - r/c_0$ is the retarded time. The result is drawn in solid line in the same figure. Both calculations are in agreement in the low-frequency part, up to 10 kHz, which validates the assumption acoustically compact surface made in the second method. Furthermore, with the sample frequency being higher for the estimation based on the lift coefficient, a hump at 50 kHz can be now

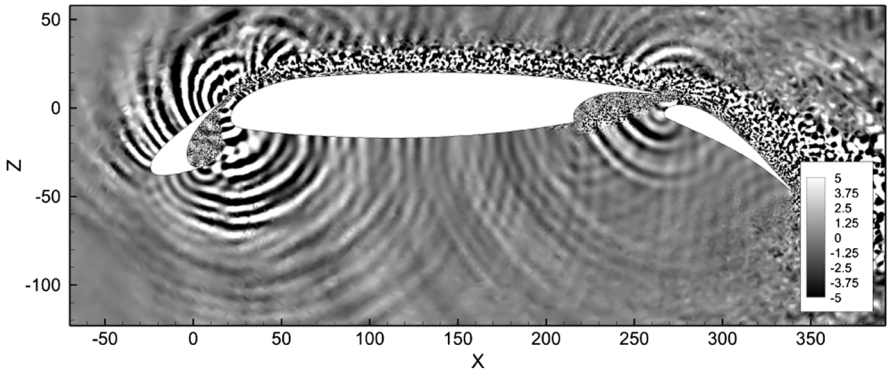

Fig. 20 Snapshot of the divergence of the fluctuating velocity field $\nabla \cdot \boldsymbol{u}^*$ in per second.

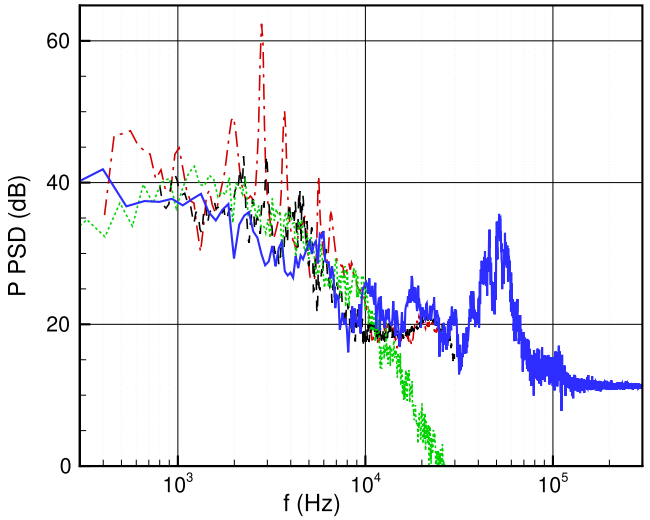

Fig. 21 PSD ($p_{ref} = 2 \times 10^{-5}$ Pa) of the radiated sound field. Simulations: VMS–Curle (dotted line), VMS–Curle for compact surfaces (solid line). Measurements: F2 ONERA (dashed line), AWB DLR-ONERA (dash-dotted line).

recorded, corresponding to a Strouhal number value of $St = 0.2$ associated with the von Kármán vortex shedding. Measurements are also reported in Fig. 21, in following the benchmark recommendations to take account of the variation of the spanwise length and other installation effects. Microphone number 4, located at the center of the (ONERA) antenna [34], has been chosen. There is an overall good agreement between these experimental data and the numerical predictions, in particular for the numerical results obtained with the assumption of compact surfaces. The frequency range 0–30 kHz of the experiments does not allow detection of the vortex shedding. The shedding frequency will be shifted to a lower audible frequency for a full-scale plane with a longer chord. Tonal peaks are also present at lower frequencies, about 1 kHz, in both experiments, especially for the AWB data. As already mentioned, the presence of such peaks strongly depends on the incidence angle. This is well illustrated here by the discrepancy between the measurements in the two wind tunnels F2 and AWB. The emergence of peaks is associated with the impingement of the shear layer in the slat cove, which is reinforced for particular values of the angle of attack. The present numerical simulations appear to be closer to the effective F2 configuration, that is, without dominant tonal noise.

Finally, the directivity of the radiated sound field has been computed from both large-eddy simulations based on the VMS and the selective Smagorinsky models. The results are plotted in Fig. 22.

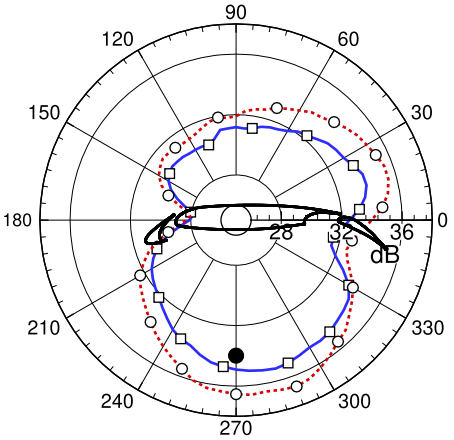

Fig. 22 Directivity of the radiated sound field: VMS model (solid line), and selective Smagorinsky model (dotted line).

A dipolar pattern can be observed, with a minimum at $\theta = 180$ deg in the upstream direction and a maximum at $\theta \simeq -70$ deg. The directivity slightly depends on the presence of the freestream M_∞ and of the angle of attack α. The numerical estimations obtained with the selective Smagorinsky model [21] systematically overpredict those of the VMS model, and thus of the experimental data by referring to Fig. 21, by a factor of 2–3 dB.

V. Conclusions

In this study, a high-order VMS subgrid model including an explicit filtering is proposed in the framework of an equal-order finite element formulation for solving the compressible Navier–Stokes equation recast for entropy variables. The filtering procedure based on embedded polynomial interpolation functions appears to be a good compromise between accuracy and efficiency, and its implementation is made easier by the use of isoparametrical and symmetrical elements. A DES-like formulation is also proposed to be able to investigate realistic flow configurations. The VMS model has been assessed by computing the Taylor–Green vortex, and the dissipation mechanisms involved in this model have been clearly identified.

A DES-like formulation is also proposed to be able to investigate industrial flow configurations. Original numerical results have been obtained with the study of the LEISA-2 problem, a high-lift system introduced in the framework of the BANC. From a numerical point of view, the hybrid VMS model provides good numerical results, by selecting the right flow areas when the explicit filtering is involved. In addition, the flow resolution near the wall is not significantly deteriorated. The VMS hybrid model is able to recover the physical effects occurring inside the slat cavity and predicts good results in terms of spectral evolution for the turbulent flow and its acoustics. The evolution of the shear layer inside the cover-slat region is correctly predicted, as well as vortex pairing leading to a broadband spectrum near the impingement point, in agreement with experiments. Despite the uncertainty regarding the angle of attack, the far-field acoustic spectrum is in good agreement with the F2 experiment. The radiated noise is mainly generated by the shear-layer impingement inside the slat cavity. Furthermore, the von Kármán vortex shedding modulated by turbulent structures coming from this impingement region has also been captured. Finally, a direct noise computation of this three-element high-lift airfoil has been performed with an original finite element flow solver.

Acknowledgments

The thesis of Pierre Yser has been funded by the French National Association of Research and Technology and the aircraft maker Dassault Aviation (Saint-Cloud, France). All the computations were made thanks to the High-Performance Computing (HPC) resources from Dassault Aviation cluster.

References

[1] Deck, S., "Recent Improvements in Zonal Detached Eddy Simulation (ZDES) Formulation," *Theoretical and Computational Fluid Dynamics*, Vol. 26, No. 6, 2012, pp. 523–550. doi:10.1007/s00162-011-0240-z

[2] Spalart, P., and Allmaras, S., "A One-Equation Turbulence Model for Aerodynamic Flows," *30th Aerospace Sciences Meeting and Exhibit*, AIAA Paper 1992-0439, 1992. doi:10.2514/6.1992-439

[3] Nikitin, N. V., Nicoud, F., Wasistho, B., Squires, K., and Spalart, P., "An Approach to Wall Modeling in Large-Eddy Simulations," *Physics of Fluids*, Vol. 12, No. 7, 2000, pp. 1629–1632. doi:10.1063/1.870414

[4] Spalart, P., Deck, S., Shur, M., Squires, K., Strelets, M. K., and Travin, A., "A New Version of Detached-Eddy Simulation, Resistant to Ambiguous Grid Densities," *Theoretical and Computational Fluid Dynamics*, Vol. 20, No. 3, 2006, pp. 181–195. doi:10.1007/s00162-006-0015-0

[5] Hughes, T. J., Feijóo, G. R., Mazzei, L., and Quincy, J.-B., "The Variational Multiscale Method—A Paradigm for Computational Mechanics," *Computer Methods in Applied Mechanics and*

Engineering, Vol. 166, Nos. 1–2, 1998, pp. 3–24.
doi:10.1016/S0045-7825(98)00079-6

[6] Hughes, T. J. R., Mazzei, L., Oberai, A. A., and Wray, A. A., "The Multiscale Formulation of Large Eddy Simulation: Decay of Homogeneous Isotropic Turbulence," *Physics of Fluids*, Vol. 13, No. 2, 2001, pp. 505–512.
doi:10.1063/1.1332391

[7] Hughes, T. J., Scovazzi, G., and Franca, L. P., "Multiscale and Stabilized Methods," *Encyclopedia of Computational Mechanics*, Wiley, New York, 2007, pp. 239–254.
doi:10.1002/9781119176817.ecm2051

[8] Sagaut, P., and Levasseur, V., "Sensitivity of Spectral Variational Multiscale Methods for Large-Eddy Simulation of Isotropic Turbulence," *Physics of Fluids*, Vol. 17, No. 3, 2005, Paper 035113.
doi:10.1063/1.1863243

[9] Levasseur, V., Sagaut, P., Chalot, F., and Davroux, A., "An Entropy-Variable-Based VMS/GLS Method for the Simulation of Compressible Flows on Unstructured Grids," *Computer Methods in Applied Mechanics and Engineering*, Vol. 195, Nos. 9–12, 2006, pp. 1154–1179.
doi:10.1016/j.cma.2005.04.009

[10] Shur, M. L., Spalart, P. R., Strelets, M. K., and Travin, A. K., "An Enhanced Version of DES with Rapid Transition from RANS to LES in Separated Flows," *Flow Turbulence and Combustion*, Vol. 95, No. 4, 2015, pp. 709–737.
doi:10.1007/s10494-015-9618-0

[11] Manoha, E., and Pott-Pollenske, M., "LEISA2: An Experimental Database for the Validation of Numerical Predictions of Slat Unsteady Flow and Noise," *21st AIAA/CEAS Aeroacoustics Conference*, AIAA Paper 2015-3137, 2015.
doi:10.2514/6.2015-3137

[12] Mallet, M., "A Finite Element Method for Computational Fluid Dynamics," Ph.D. Thesis, Stanford Univ., Stanford, CA, 1985.

[13] Hughes, T. J. R., Scovazzi, G., and Franca, L. P., "Stabilized Methods for Compressible Flows," *Journal of Scientific Computing*, Vol. 43, No. 3, 2010, pp. 343–368.
doi:10.1007/s10915-008-9233-5

[14] Hughes, T., *The Finite Element Method: Linear Static and Dynamic Finite Element Analysis*, Prentice–Hall, 1987.
doi:10.1111/j.1467-8667.1989.tb00025.x

[15] Chalot, F. L., and Perrier, P., "Industrial Aerodynamics," *Encyclopedia of Computational Mechanics*, Wiley, 2004.
doi:10.1002/0470091355.ecm065

[16] Hughes, T., Franca, L. P., and Hulbert, G. M., "A New Finite Element Formulation for Computational Fluid Dynamics: 8. The Galerkin/Least-Squares Method for Advective-Diffusive Equations," *Computer Methods in Applied Mechanics and Engineering*, Vol. 73, No. 2, 1989, pp. 173–189.
doi:10.1016/0045-7825(89)90111-4

[17] Sagaut, P., *Large Eddy Simulation for Incompressible Flows: An Introduction*, Springer–Verlag, Berlin, 2006, Chap. 2.
doi:10.1007/b137536

[18] Erlebacher, G., Hussaini, M. Y., Speziale, C. G., and Zang, T. A., "Toward the Large Eddy Simulation of Compressible Turbulent Flow," *Journal of Fluid Mechanics*, Vol. 238, May 1992, pp. 155–185.
doi:10.1017/S0022112092001678

[19] Bailly, C., and Comte-Bellot, G., *Turbulence*, Springer, 2015, Chap. 8.
doi:10.1007/978-3-319-16160-0

[20] Meyers, J., and Sagaut, P., "On the Model Coefficients for the Standard and the Variational Multi-Scale Smagorinsky Model," *Journal of Fluid Mechanics*, Vol. 569, Dec. 2006, pp. 287–319.
doi:10.1017/S0022112006002850

[21] Levasseur, V., Sagaut, P., and Mallet, M., "Subgrid Models for Large-Eddy Simulation Using Unstructured Grids in a Stabilized Finite Element Framework," *Journal of Turbulence*, Vol. 28, No. 7, 2006, pp. 1–16.
doi:10.1080/14685240600600352

[22] Lesieur, M., and Métais, O., "New Trends in Large-Eddy Simulations of Turbulence," *Annual Review of Fluid Mechanics*, Vol. 28, No. 1, 1996, pp. 45–82.
doi:10.1146/annurev.fl.28.010196.000401

[23] Lilly, D., "A Proposed Modification on the Germano Subgrid-Scale Closure Method," *Physics of Fluid A*, Vol. 4, No. 3, 1992, pp. 633–635.
doi:10.1063/1.858280

[24] Bogey, C., and Bailly, C., "Decrease of the Effective Reynolds Number with Eddy-Viscosity Subgrid-Scale Modelling," *AIAA Journal*, Vol. 43, No. 2, 2005, pp. 437–439.
doi:10.2514/1.10665

[25] Vasilyev, O. V., Lund, T. S., and Moin, P., "A General Class of Commutative Filters for LES in Complex Geometries," *Journal of Computational Physics*, Vol. 146, No. 1, 1998, pp. 82–104.
doi:10.1006/jcph.1998.6060

[26] Najafi-Yazdi, A., Najafi-Yazdi, M., and Mongeau, L., "A High Resolution Differential Filter for Large Eddy Simulation: Toward Explicit Filtering on Unstructured Grids," *Journal of Computational Physics*, Vol. 292, July 2015, pp. 272–286.
doi:10.1016/j.jcp.2015.03.034

[27] Brazell, M. J., Brazell, M., Stoellinger, M., Mavriplis, D. J., and Kirby, A., "Using LES in a Discontinuous Galerkin Method with Constant and Dynamic SGS Models," *53rd AIAA Aerospace Sciences Meeting*, AIAA Paper 2015-0060, 2015, pp. 1–18.
doi:10.2514/6.2015-0060

[28] Uribe, J. C., Jarrin, N., Prosser, R., and Laurence, D., "Development of a Two-Velocities Hybrid RANS-LES Model and Its Application to a Trailing Edge Flow," *Flow Turbulence and Combustion*, Vol. 85, No. 2, 2010, pp. 181–197.
doi:10.1007/s10494-010-9263-6

[29] Xiao, H., and Jenny, P., "A Consistent Dual-Mesh Framework for Hybrid LES/RANS Modeling," *Journal of Computational Physics*, Vol. 231, No. 4, 2012, pp. 1848–1865.
doi:10.1016/j.jcp.2011.11.009

[30] Fauconnier, D., "Development of a Dynamic Finite Difference Method for Large-Eddy Simulation," Ph.D. Thesis, Ghent Univ., Ghent, Belgium, 2008.

[31] Brachet, M., Meiron, D., Orszag, S., Nickel, B., Morf, R., and Frisch, U., "Small-Scale Structure of the Taylor–Green Vortex," *Journal of Fluid Mechanics*, Vol. 130, May 1983, pp. 411–452.
doi:10.1017/S0022112083001159

[32] Jeong, J., and Hussain, F., "On the Identification of a Vortex," *Journal of Fluid Mechanics*, Vol. 285, Feb. 1995, pp. 69–94.
doi:10.1017/S0022112095000462

[33] Yser, P., "Simulation Numérique Aéroacoustique d'Écoulements par une Approche LES d'Ordre Élevé en Éléments Finis non Structurés," Ph.D. Thesis, École Centrale de Lyon, Lyon, France, Jan. 2017 (in French).

[34] "Low-Noise Exposure Integrated Design for Start and Approach. Benchmark for Airframe Noise Computations Category 6. Database Description," Ver. 1, DLR, German Aerospace Center, TR, Chatillon, France, 2014.

[35] Dobrzynski, W., "Almost 40 Years of Airframe Noise Research: What Did We Achieve?" *Journal of Aircraft*, Vol. 47, No. 2, 2010, pp. 353–367.
doi:10.2514/1.44457

[36] Choudhari, M., and Khorrami, M., "Effect of Three Dimensional Shear Layer Structures on Slat Cove Unsteadiness," *AIAA Journal*, Vol. 45, No. 9, 2007, pp. 2174–2186.
doi:10.2514/1.24812

[37] Reuß, S., Knopp, T., and Schwamborn, D., "Investigation of the Resolution Requirements for a Hybrid RANS/LES Simulation of a Multi-Element Airfoil," *Computational Flight Testing*, edited by N. Kroll, R. Radespiel, J. Burg, and K. Sørensen, Springer, Berlin, 2013, pp. 43–57.
doi:10.1007/978-3-642-38877-4_4

[38] Deck, S., and Laraufie, R., "Numerical Investigation of the Flow Dynamics Past a Three-Element Aerofoil," *Journal of Fluid Mechanics*, Vol. 732, Oct. 2013, pp. 401–444.
doi:10.1017/jfm.2013.363

[39] Terracol, M., Manoha, E., and Lemoine, B., "Investigation of the Unsteady Flow and Noise Generation in a Slat Cove," *AIAA Journal*, Vol. 54, No. 2, 2016, pp. 469–489.
doi:10.2514/1.J053479

[40] Zhang, Y., Chen, H., Wang, K., and Wang, M., "Aeroacoustic Prediction of a Multi-Element Airfoil Using Wall-Modeled Large-Eddy Simulation," *AIAA Journal*, Vol. 55, No. 12, 2017, pp. 4219–4233.
doi:10.2514/1.J055853

[41] Perraud, J., Arnal, D., Casalis, G., Archambaud, J.-P., and Donelli, R., "Automatic Transition Predictions Using Simplified Methods," *AIAA Journal*, Vol. 47, No. 11, 2009, pp. 2676–2684.
doi:10.2514/1.42990

[42] Khorrami, M. R., Singer, B., and Berkman, M., "Time-Accurate Simulations and Acoustic Analysis of Slat Free-Shear Layer," *AIAA Journal*, Vol. 40, No. 7, 2002, pp. 1284–1291.
doi:10.2514/2.1817

[43] Terracol, M., Labourasse, E., Manoha, E., and Sagaut, P., "Simulation of the 3D Unsteady Flow in a Slat Cove for Noise Prediction," *9th AIAA/CEAS Aeroacoustics Conference and Exhibit*, AIAA Paper 2003-3110, May 2003.
doi:10.2514/6.2003-3110

[44] Gloerfelt, X., Pérot, F., Bailly, C., and Juvé, D., "Flow-Induced Cylinder Noise Formulated as Diffraction Problem for Low Mach Number Flows," *Journal of Sound and Vibration*, Vol. 287, Nos. 1–2, 2005, pp. 129–151.
doi:10.1016/j.jsv.2004.10.047

D. Gaitonde
Associate Editor